

## Analysis of time-domain back-projection for stripmap SAR

Michael I Duersch\* and David G Long

*Electrical and Computer Engineering, Brigham Young University, Provo, UT, USA*

*(Received 17 October 2014; accepted 16 February 2015)*

This article explores the SAR back-projection algorithm for stripmap image formation and its characteristics. The article provides a derivation of generalized time-domain back-projection from first principles. It shows that back-projection may be considered an ideal matched filter for SAR. The article presents an analysis of the sensitivity of back-projection to its geometric parameters as well as several performance considerations: azimuth beam width, residual phase error, digital elevation map accuracy, and antenna position estimation accuracy.

### 1. Introduction

Synthetic aperture radar (SAR) utilizes platform motion to obtain finer resolution in the along-track dimension than that given by the along-track illumination footprint (Cumming and Wong 2005). In order to form images from the raw SAR phase history data, researchers have developed many different algorithms (Cumming and Bennett 1979; Jin and Wu 1984; Rocca 1987; Raney et al. 1994; Eldhuset 1998; Moreira, Mittermayer, and Scheiber 1996; Mittermayer, Moreira, and Loffeld 1999). Most SAR algorithms are based on the use of frequency domain techniques and have been analysed in detail (Cumming and Wong 2005; Bamler 1992; Carrara, Goodman, and Majewski 1995; Benz, Strodl, and Moreira 1995; Caves, Quegan, and White 1998; Gilmore, Jeffrey, and LoVetri 2006; Prats et al. 2007; Zaugg and Long 2009). More recent articles have explored modifications to frequency domain techniques that allow for high-resolution imaging (Ulander, Hellsten, and Stenstrom 2003; D’Aria and Guarnieri 2007, Sun et al. 2011; Prats-Iraola et al. 2014; Rodriguez-Cassola et al. 2015). Time-domain back-projection for SAR has been less studied (Ulander, Hellsten, and Stenstrom 2003; Zaugg and Long 2015).

This article seeks to provide a more detailed analysis of the time-domain back-projection image formation algorithm than presently available in the literature, including characterization of the sensitivities of back-projection to its various parameters. The article considers the sources of error and provides analysis of requirements to achieve a given level of performance. In order to facilitate this, we begin with a generalized derivation of the time-domain back-projection algorithm and analysis of when approximations may be made to reduce computational burden.

### 2. Generalized time-domain back-projection

Some SAR image formation derivations begin with two implicit assumptions: that the radar point spread function is constant across the image and that image formation may be

---

\*Corresponding author. Email: [mid@byu.net](mailto:mid@byu.net)

separated into two steps – range compression and azimuth compression (Cumming and Wong 2005; Bamler 1992). This equates to formulating the problem into one of convolution. Since this is only an approximation, in order to be more general, we explicitly avoid this assumption.

The following subsections provide a detailed derivation of the stripmap time-domain back-projection image formation algorithm. We begin with a general, time-domain, uncompressed formulation and then progress to other forms through the use of various assumptions. These results are used in later sections as the basis for the back-projection analysis.

### 2.1. Derivation of general form

We begin with a generic linear frequency modulated (LFM) transmit signal:

$$\begin{aligned} s^{\text{tx}}(t) &= w(t) \exp\{j2\pi\phi(t)\}, \\ &= w(t) \exp\left\{\underbrace{j2\pi f_0 t}_{\text{propagation phase}} + \underbrace{j\pi K t^2}_{\text{FM chirp}} + j\phi_0\right\}, \end{aligned} \quad (1)$$

where  $\phi(t)$  is the LFM phase,  $t$  is fast-time,  $f_0$  is the centre frequency, and  $K$  is the frequency modulation (FM) ramp-rate in Hz per second,  $\phi_0$  is the initial phase, and  $w(t)$  is the pulse envelope (e.g.  $w(t) = \text{rect}(t/T) = 1$  over the domain  $t/T \in [-\frac{1}{2}, \frac{1}{2}]$ , with  $T$  the pulse duration).

Consider a stationary, isotropic scatterer located in three-space. The round-trip propagation delay from transmitter to scatterer to receiver is  $t_n$ , where  $n$  is the slow-time pulse index. Note that  $t_n$  is implicitly a function of fast-time  $t$  (as a result of platform motion during a pulse), but for simplicity this is not included in notation. From Equation (1), the scattered received signal is an amplitude-adjusted, time-delayed copy of the transmit signal:

$$\begin{aligned} s_n^{\text{rx}}(t) &= A_n(t - t_n) G_n(t - t_n) w(t - t_n) \\ &\quad \cdot \exp\left\{j2\pi f_0(t - t_n) + j\pi K(t - t_n)^2 + j\phi_0\right\} + \eta. \end{aligned} \quad (2)$$

Here,  $A_n(t)$  is an amplitude term that depends on target area, atmospheric effects, etc.,  $G_n(t)$  is an amplitude term dependent on antenna gains, propagation loss, system filters, etc., and  $\eta$  is additive noise. When the received signal is demodulated this becomes

$$s_n^{\text{rx}}(t) = A_n(t - t_n) G_n(t - t_n) w(t - t_n) \exp\left\{-j2\pi f_0 t_n + j\pi K(t - t_n)^2 + j\phi_0\right\} + \eta. \quad (3)$$

Examining this equation, the first term inside the exponential is the propagation phase while the second term inside the exponential is the LFM chirp.

As the energy of the received signal is spread in fast- and slow-times, it is desirable to focus this energy as narrowly as possible. This process is known as *compression*. Compression is performed with a matched filter since it maximizes signal-to-noise ratio in the presence of additive noise Richards (2005) (although other types of filters could be used, e.g. a Wiener filter). To matched-filter Equation (3), the filter reference function is

$$h_n^C(t) = w(t - \tilde{t}_n) G_n(t - \tilde{t}_n) \exp\left\{-j2\pi f_0 \tilde{t}_n + j\pi K(t - \tilde{t}_n)^2\right\}, \quad (4)$$

where  $\tilde{t}_n$  is the delay parametrizing the matched filter. Ideally  $\tilde{t}_n$  is equal to  $t_n$ , but it is retained as a separate term to explore the results of mismatch.

Matched filtering is often implemented through the use of correlation (i.e. sliding inner-product). However, this concept is not fully congruous with the concept of back-projection because the kernel is not constant (i.e. it changes with position). By calculating each pixel individually, the filter is tailored to match the conditions of that pixel. This becomes especially advantageous in very low-altitude, high-motion environments Duersch and Long (2015).

Neglecting the noise term for the sake of brevity, the result of matched filtering a single pixel is

$$\begin{aligned} I &= \sum_{n \in \mathcal{N}} \int s_n^{\text{rx}}(\tau) h_n^{C*}(\tau) d\tau \quad (5) \\ &= \sum_{n \in \mathcal{N}} \int A_n(\tau - t_n) G_n(\tau - t_n) w_n(\tau - t_n) \\ &\quad \cdot \exp\left\{-j2\pi f_0 t_n + j\pi K(\tau - t_n)^2 + j\phi_0\right\} \\ &\quad \cdot G_n(\tau - \tilde{t}_n) w_n(\tau - \tilde{t}_n) \exp\left\{j2\pi f_0 \tilde{t}_n - j\pi K(\tau - \tilde{t}_n)^2\right\} d\tau, \quad (6) \end{aligned}$$

where  $\mathcal{N}$  is the set of all pulses contributing to the pixel and  $I$  is the pixel value. Note the lack of a conjugation symbol  $*$  on  $G()$  and  $w()$ , which are assumed to be purely real-valued.

Several observations are in order. First, matched filtering in this manner handles both propagation phase and the LFM chirp, thus simultaneously performing both azimuth and range compression, respectively. Second, gain variation in both fast- and slow-time can be expressed since  $G_n(t)$  and  $w_n(t)$  are functions of both. Third, Equation (6) yields the value  $I$  for only a single pixel: this process must be repeated for a grid of pixels representing the desired image. Performing this process on an  $n \times n$  image is computationally expensive, on the order of  $\mathcal{O}(n^4)$ . Note that in the formulation presented here, the grid of pixels is defined in the ground-plane, not the slant-plane.

In the model above, the scatterer is a single point target. In general however, a pixel may contain simultaneous contributions from multiple scatterers within a given area/volume whose size is bounded by the single-look resolution of the SAR. This volume is termed a *scattering-cell*. For a single pulse, the superposition of all the scatterers inside the scattering-cell is often treated as a single point target. However, the superposition of the scatterers may have a phase-centre offset  $\delta$  from the geometric centre of the scattering-cell. Depending on the nature of the cell, the amplitude and phase of summed scatterers may not be constant over slow-time.

If  $\tilde{t}_n = t_n$ , the pixel value is

$$I = \exp(j\phi_0) \sum_{n \in \mathcal{P}} \int A_n(\tau - t_n) G_n^2(\tau - t_n) w_n^2(\tau - t_n) d\tau. \quad (7)$$

With the assumption that the time delay to the target is known exactly for every pulse, the phase of the filter perfectly matches the phase of the signal. For this to hold, the target phase-centre must be located at precisely the anticipated position; it is not sufficient to use the delay to the centre of the scattering-cell, but rather the delay to the phase-centre of the scattering-cell (for each pulse). Unfortunately, the physical centre and phase-centre of a scattering-cell are not collocated in general. This leads to a phase error when the matched filter is set to the range to the centre of the cell.

If  $t_n \neq \tilde{t}_n$  due to the phase-centre offset, then the complex exponentials in Equation (6) do not cancel out and a differential propagation phase results:  $\exp\{j2\pi f_0(\tilde{t}_n - t_n)\}$ . There is also an error  $\phi_{\text{LEM error}}$  due to mismatch in the LFM chirp term; however, for SAR systems with a typical LFM time-bandwidth product ( $> 100$ ), the chirp mismatch  $\phi_{\text{LEM error}}$  is insignificant (Cumming and Wong 2005). The resulting pixel value is

$$I = \exp(j\phi_0) \sum_{n \in P} \int A_n(\tau - t_n) G_n^2(\tau - t_n) w_n^2(\tau - t_n) \exp\{j2\pi f_0(\tilde{t}_n - t_n)\} d\tau. \quad (8)$$

The differential propagation phase term is critical and is termed the *residual phase*. Residual phase plays a critical role in the back-projection analysis presented in later sections.

## 2.2. Compression simplification

As stated above, simultaneously performing range and azimuth compression according to Equation (6) is computationally very expensive. However, under many conditions compression can be broken into two separate steps (range and azimuth compression). The limiting factor preventing separation in the derivation above is the implicit dependence of  $t_n$  on fast-time. However, if the pulse duration  $T$  is short enough that the platform movement during propagation is insignificant, then  $t_n$  may be considered fixed for a given pulse duration. This is the classic *stop-and-hop* approximation.

When this assumption applies, the matched filter may be modified to first perform range compression by using the reference function

$$h_n^R(t) = w(t - t_n) \exp\{j\pi K(t - t_n)^2\}, \quad (9)$$

which includes only the LFM chirp term. This leads to the range-compressed (matched filtered) signal  $g_n(t)$ :

$$g_n(t) = \int s_n^{\text{rx}}(\tau) h_n^{\text{R}*}(\tau - t) d\tau \quad (10)$$

$$= \int A_n(\tau - t_n) G_n(\tau - t_n) w(\tau - t_n) \exp\{-j2\pi f_0 t_n + j\pi K(\tau - t_n)^2 + \phi\} \\ \cdot w(\tau - t - \tilde{t}_n) \exp\{-j\pi K(\tau - t - \tilde{t}_n)^2\} d\tau. \quad (11)$$

When  $w(t) = \text{rect}(t/T)$ , this is approximately

$$g_n(t) \approx A_n(t - t_n) G_n(t - t_n) T \text{sinc}\{KT(t - (\frac{t_n^2}{n} - \tilde{t}_n^2))\} \exp\{-j2\pi f_0 t_n + \phi\}. \quad (12)$$

At this point it is useful to map this result from time coordinates to spatial coordinates. This is done by noting that the two-way delay is

$$t_n = \frac{r_n^{\text{tx}} + r_n^{\text{rx}}}{c}, \quad (13)$$

where  $r_n^{\text{tx}}$  and  $r_n^{\text{rx}}$  are the transmitter and receiver range-to-target, respectively. In the case of a monostatic radar,  $r_n^{\text{tx}} = r_n^{\text{rx}}$ . The propagation phase term in Equation (12) is equivalent to

$$2\pi f_0 t_n = k(r_n^{\text{tx}} + r_n^{\text{rx}}), \quad (14)$$

where

$$k = 2\pi f_0 / c = 2\pi / \lambda. \quad (15)$$

The two-way range to the target is

$$d_n = r_n^{\text{tx}} + r_n^{\text{rx}}, \quad (16)$$

while the two-way range parametrizing the matched filter is  $\tilde{d}_n$ . The difference between the two is the two-way *residual range*:

$$\Delta d_n = \tilde{d}_n - d_n. \quad (17)$$

The phase-centre may be anywhere in the scattering-cell. In the ‘worst case’ scenario, it may be in the corner of the scattering-cell which results in maximum residual range. This is illustrated in Figure 1, where point  $p$  is maximally displaced from the centre of the cell at point  $o$ . Thus, the maximum horizontal (i.e. ground-range) displacement of a target in the scattering-cell is half the ground-resolution cell width:

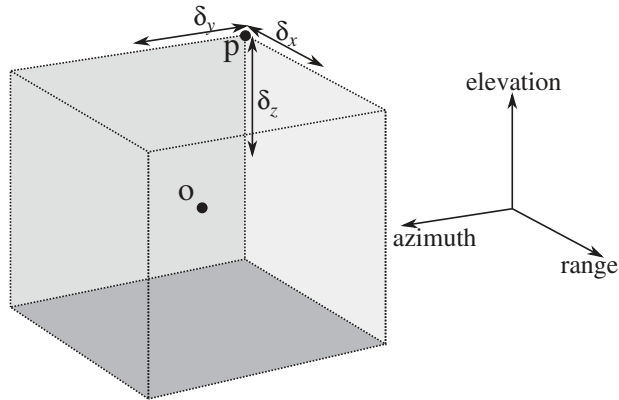


Figure 1. Illustration of a scattering-cell. Point  $o$  is the physical centre of the cell and point  $p$  is the phase-centre. In this diagram, the phase-centre is maximally displaced from the physical centre of the cell.  $\delta_x$ ,  $\delta_y$ , and  $\delta_z$  represent the phase-centre displacement in azimuth, range, and elevation, respectively.

$$\delta_{y-\max} = \frac{R_g}{2} = \frac{R_y}{2 \sin \theta}, \quad (18)$$

with  $R_y$  the slant-range resolution and  $R_g$  the ground-range resolution. The maximum vertical displacement (at the centre of the cell) is

$$\delta_{z-\max} = R_y \cos \theta. \quad (19)$$

The maximum azimuth displacement is half the azimuth resolution:

$$\delta_{x-\max} = R_x/2.$$

Recall that these are the worst-case scenarios. The expected position of the phase-centre of a distributed target is near the cell's centre. However, a point target such as a corner reflector may truly be located at the edge of the scattering-cell.

Using the mapping of time to distance, the range-compressed signal may be written as

$$g_n(l) = A_n(l - d_n) G_n(l - d_n) R(\Delta d_n) \exp\{-jk d_n\}, \quad (20)$$

where  $l$  is fast-time distance and  $R(l)$  is the range-compressed impulse response centred at  $l = 0$ .

Azimuth compression of the range-compressed signal in Equation (20) is computed by matched-filtering the range-compressed signal with the reference function:

$$h_n^A(t) = w_n \exp(-jk \tilde{d}_n), \quad (21)$$

where  $w_n$  is an optional slow-time window function. This leads to the back-projected result

$$\begin{aligned} I &= \sum_{n \in \mathcal{N}} g_n(\tilde{d}_n) w_n \exp(jk \tilde{d}_n) \\ &= \sum_{n \in \mathcal{N}} A_n(\Delta d_n) G_n(\Delta d_n) R(\Delta d_n) w_n \exp(jk \Delta d_n). \end{aligned} \quad (22)$$

In practice, amplitude terms such as antenna gain may be included in  $w_n$ . The phase term  $\exp(jk \Delta d_n)$  is the residual propagation phase present at each pulse when  $\Delta d_n \neq 0$ . Performing range and azimuth separately in this manner leads to a computational complexity of  $\mathcal{O}(n^3)$  for an  $n \times n$  image. Further simplification, albeit with some loss of quality, may be obtained through fast-factorized back-projection (Vu, Sjogren, and Pettersson 2008, 2011).

In the stop-and-hop derivation above, the antennas are considered stationary through the duration of the pulse. If the antennas move significantly (on the order of a wavelength or more) during the pulse, range/azimuth compression is still separable if the platform velocity is constant. A derivation of this is shown in Ribalta (2011). A modification for LFM-CW (continuous wave) operation is given in Zaugg (2010).

### 3. Range-to-target

One of the key parameters in the back-projection equation is the distance (or equivalently, the time delay) from the antenna(s) to the scattering-cell phase-centre. Since the precise location of the phase-centre is unknown, the assumed distance is that to the physical centre of the cell. The assumed distance is based on the pixel grid and parameterizes the back-projection matched filter. It is the difference between the assumed and actual distances that leads to the residual distance  $\Delta d_n$  (and residual phase  $k\Delta d_n$ ) discussed previously.

Define the *nominal residual phase* for a given target as the residual phase at the mean position of the synthetic aperture, which is ideally the point of closest approach (POC). Contributing samples from pulses transceived away from the mean position may have a different residual phase than the nominal. The difference between the residual phase at surrounding pulses and the nominal at the POC is the *phase error*. In general, the phase error increases as the platform distance from the mean position increases. If the phase error becomes too large then the contributing sample sums destructively during back-projection summation. In order to facilitate later sensitivity and performance analysis of back-projection, we examine the residual range that leads to the residual phase.

With the dimensions  $x, y, z$  as along-track, cross-track, and elevation, respectively, the one-way range  $r_n$  to the physical centre of a scattering-cell is

$$\begin{aligned} r_n &= \sqrt{x_n^2 + y_n^2 + z_n^2} \\ &= \sqrt{(\bar{x} + \varsigma_{x,n})^2 + (\bar{y} + \varsigma_{y,n})^2 + (\bar{z} + \varsigma_{z,n})^2} \\ &= \sqrt{(\bar{x}^2 + \bar{y}^2 + \bar{z}^2) + \varsigma_{x,n}(2\bar{x} + \varsigma_{x,n}) + \varsigma_{y,n}(2\bar{y} + \varsigma_{y,n}) + \varsigma_{z,n}(2\bar{z} + \varsigma_{z,n})}, \end{aligned} \quad (23)$$

where  $n$  is the time index. The variables  $\bar{x}, \bar{y}$ , and  $\bar{z}$  are the mean ranges-to-target in their respective dimensions. For example,  $\bar{x}$  is zero for non-squinted geometry, as illustrated in Figure 2. The variables  $\varsigma_{x,n}, \varsigma_{y,n}$ , and  $\varsigma_{z,n}$  are the antenna displacements from the mean at time  $n$ . Finally,  $x_n, y_n$ , and  $z_n$  are the ranges from the antenna to the scattering-cell for each time index. They are equal to the sum of the mean range-to-target and the antenna displacement from the mean (e.g.  $x_n = \bar{x} + \varsigma_{x,n}$ ).

The range to the phase-centre  $r'_n$  is

$$\begin{aligned} r'_n &= \sqrt{x'_n{}^2 + y'_n{}^2 + z'_n{}^2} \\ &= \sqrt{(\bar{x} + \varsigma_{x,n} - \delta_x)^2 + (\bar{y} + \varsigma_{y,n} - \delta_y)^2 + (\bar{z} + \varsigma_{z,n} - \delta_z)^2} \\ &= \sqrt{(\bar{x}^2 + \bar{y}^2 + \bar{z}^2) + V_{x,n} + V_{y,n} + V_{z,n}}, \end{aligned} \quad (24)$$

with the azimuth terms grouped into

$$V_{x,n} = \varsigma_{x,n}^2 + \delta_x^2 + 2(\bar{x}\varsigma_{x,n} - \bar{x}\delta_x) \quad (25)$$

and likewise  $V_{y,n}$  and  $V_{z,n}$  for the range and elevation terms. Note that as  $\varsigma_{y,n}$  and  $\varsigma_{z,n}$  are in general non-zero, the model accounts for non-ideal motion and does not require a strictly hyperbolic range-to-target.

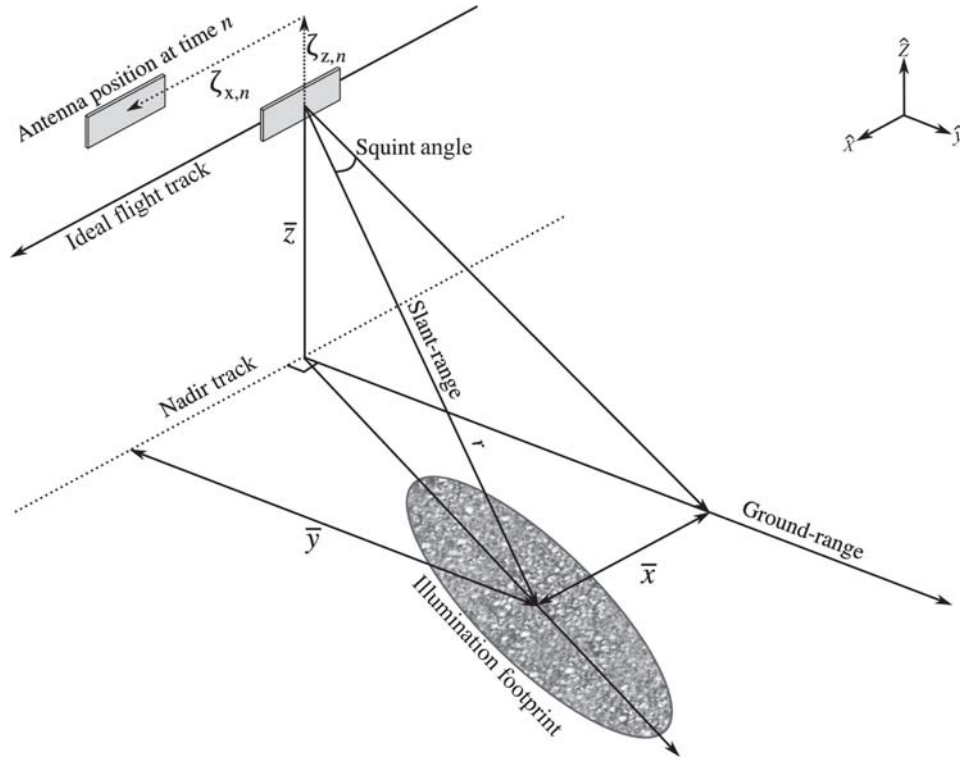


Figure 2. SAR geometry.  $\bar{x}$ ,  $\bar{y}$ , and  $\bar{z}$  are the mean azimuth, range, and elevation ranges, respectively, to the target.  $\zeta_{x,n}$ ,  $\zeta_{y,n}$  (not shown), and  $\zeta_{z,n}$  are the antenna displacements from the mean at time  $n$ .

Given the ranges defined above, the one-way residual range is

$$\Delta r_n = r_n - r'_n \tag{26}$$

$$= \sqrt{x_n^2 + y_n^2 + z_n^2} - \sqrt{x_n'^2 + y_n'^2 + z_n'^2}. \tag{27}$$

The residual range leads to the phase term  $2k\Delta r_n$  present at each pulse summed in back-projection (assuming a monostatic radar). A non-zero value for  $\Delta r_n$  results in residual phase. In order to analytically examine the significance of the residual range, it is necessary to manipulate Equation (27). Unfortunately, manipulation is difficult in this exact form, but becomes tractable with approximation techniques. Several approximations are considered in the following.

### 3.1. First-order Taylor series approximation

Suppose the mean range-to-target is

$$\bar{r} = \sqrt{\bar{x}^2 + \bar{y}^2 + \bar{z}^2}. \tag{28}$$

A first-order Taylor series approximation of the square root (where  $a \gg b$ )

$$\sqrt{a^2 + b} \approx a + \frac{b}{2a} \quad (29)$$

can be used in Equations (23) and (24) to produce

$$r_n \approx \bar{r} + \frac{\varsigma_{x,n}(2\bar{x} + \varsigma_{x,n}) + \varsigma_{y,n}(2\bar{y} + \varsigma_{y,n}) + \varsigma_{z,n}(2\bar{z} + \varsigma_{z,n})}{2\bar{r}}, \quad (30)$$

$$r'_n \approx \bar{r} + \frac{V_{x,n} + V_{y,n} + V_{z,n}}{2\bar{r}}. \quad (31)$$

This approximation is valid for stripmap geometries where, for a given target, the SAR does not illuminate the target when it is far from the mean range-to-target  $\bar{r}$  (i.e. a narrow beam in azimuth). With this approximation the residual range is

$$\Delta r_n = \frac{\beta_n}{2\bar{r}}, \quad (32)$$

where

$$\beta_n = 2[\delta_x(\bar{x} + \varsigma_{x,n}) + \delta_y(\bar{y} + \varsigma_{y,n}) + \delta_z(\bar{z} + \varsigma_{z,n})] - \delta_x^2 - \delta_y^2 - \delta_z^2. \quad (33)$$

A quick examination of this shows that if the phase-centre of the scattering-cell is known (i.e. the  $\delta$  terms in Equation (33) are zero) then the residual range vanishes identically, as expected.

An important observation regarding the approximation of Equation (32) is that in the case of ideal, linear motion,  $\beta_n$ , and therefore the  $\Delta r_n$  predicted using the Taylor series approximation, are constant for all  $n$  (given that  $\delta_x$  is zero). This, however, is not strictly true since  $\Delta r_n$  is the difference between two hyperbolas with separate foci. This point illustrates the limitation of the first-order Taylor series approximation: since this approximation erroneously suggests  $\phi_n$  is constant for all  $n$ , it likewise suggests there are no residual phase variations and thus no phase errors.

For low values of  $\varsigma_{x,n}$ , the phase error is small so the constant  $\Delta r_n$  approximation can be used. Hence, the first-order Taylor series is a good approximation for narrow-beam antennas and is close to the POC approach.

### 3.2. Bakhshali approximation

In order to ameliorate the restrictions of the first-order Taylor series approximation, we introduce the Bakhshali square root approximation (Channabasappa 1976). The Bakhshali method of approximating the square root is equivalent to two iterations of the first-order Taylor series approximation:

$$\sqrt{a^2 + b} \approx a + \frac{b}{2a} - \frac{b^2}{8a^3 + 4ab}. \quad (34)$$

The residual range is then

$$\Delta r_n \approx \frac{\beta_n}{2\bar{r}} - \frac{\gamma_n^2}{4\bar{r}(2\bar{r}^2 + \gamma_n)} + \frac{(\gamma_n - \beta_n)^2}{4\bar{r}(2\bar{r}^2 + \gamma_n - \beta_n)}, \quad (35)$$

with  $\beta_n$  as in Equation (33) and

$$\gamma_n = 2(\bar{x}\zeta_{x,n} + \bar{y}\zeta_{y,n} + \bar{z}\zeta_{z,n}) + \zeta_{x,n}^2 + \zeta_{y,n}^2 + \zeta_{z,n}^2. \quad (36)$$

Notice that the first term in Equation (35) is precisely the first-order Taylor series approximation in Equation (32). As in the Taylor series approximation, when  $\beta_n = 0$ , the residual range vanishes.

A comparison of both methods along with the third-order Taylor series approximation

$$\sqrt{a^2 + b} \approx a + \frac{b}{2a} - \frac{b^2}{8a^2} + \frac{b^3}{16a^3} \quad (37)$$

is illustrated in Figure 3(a). In this example, an antenna is placed at a 45° incidence angle to the scattering-cell and the phase-centre is displaced in slant-range (i.e. both range and elevation) by 1 m. The solid curve shows the exact value of the residual range. The first-order Taylor series approximation is constant at all azimuth angles. The third-order Taylor and Bakhshali methods both exhibit hyperbola-like shapes; however, the Bakhshali method is accurate over a much wider range of azimuth angles and requires fewer operations than the third-order Taylor series. The Bakhshali method becomes very useful when analysing the effects of residual range on wide-beamed antennas.

Figure 3(b) shows the approximation error of each method using the same conditions above. Incidence angles between 30° and 60° exhibit similar behaviour. How much error can be tolerated depends on the radar wavelength and expected phase-centre displacement. Radars with fine resolution relative to the wavelength better tolerate phase-centre

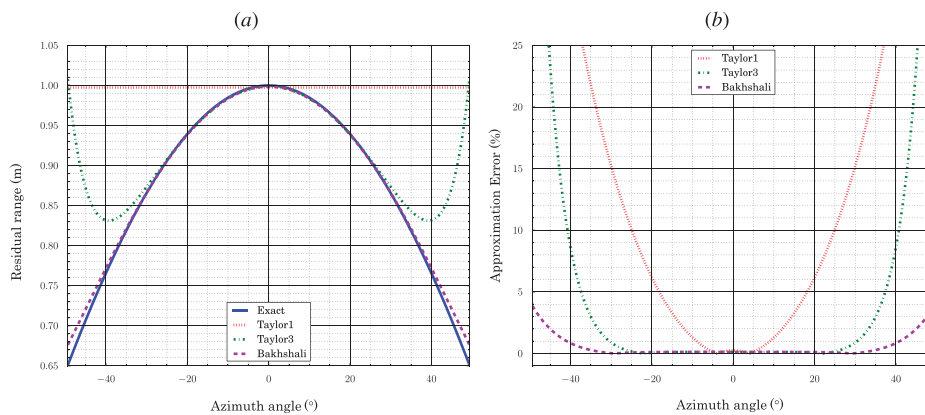


Figure 3. Comparison of the range residual approximations for varying azimuth angles-to-target with an incidence of 45°. Subfigure (a) shows the range residual where the solid curve represents the exact solution, while the dashed/dotted curves are the approximations. Note that the first-order Taylor series approximation is constant with azimuth angle. Subfigure (b) shows a comparison of the approximation error. Each of the approximations is accurate near 0° azimuth (the POC approach) but beyond that all have varying degrees of accuracy at larger angles.

displacement than those with coarse resolution. As evident from subfigure (b), antennas with up to a 20° azimuth beamwidth have about 1% error when using the first-order Taylor series approximation. Many SAR antennas in practice have such a beamwidth or even narrower. Thus, for the purposes of this article, an antenna with a beamwidth of 20° or lower is termed ‘narrow-beam’. If accuracy across a wider beamwidth is required then the Bakhshali method is preferable as the error is still small at a 90° beamwidth.

Note that these results bound the approximation error: distributed targets are unlikely to have a phase-centre near the corner of the scattering-cell because they generally have small phase-centre displacement from the centre of the cell.

### 3.3. Sensitivity

With the derived approximations in place for the square roots in the residual range formula, an analytic examination of sensitivity is possible. The sensitivity of the residual range  $\Delta r_n$  is found by solving its partial derivative with respect to each of the constituent terms. Note that while the partial derivative is taken with respect to only the azimuth dimension below, similar results hold for the other dimensions by substituting  $x$  for  $y$  and  $z$ . Thus, only one case is shown.

#### 3.3.1. Phase-centre displacement

$$\frac{\partial \Delta r_n}{\partial \delta_x} = \frac{\bar{x} + \zeta_{x,n} - \delta_x}{\bar{r}}. \quad (38)$$

The sensitivity of the residual range to phase-centre displacement determines how much the residual range changes for a given change in phase-centre displacement. This sensitivity to phase-centre displacement is greatest in whichever dimension has the largest range-to-target. For narrow-beam antennas with zero squint geometry, this is the elevation dimension at shallow incidence angles and the ground-range dimension at large incidence angles.

In a given dimension, when the antenna is located far away from its mean position (i.e.  $\bar{x}$ ,  $\bar{y}$ , or  $\bar{z}$ ), phase-centre displacement in that dimension becomes more significant. This is particularly applicable in the along-track dimension with either a squinted geometry or a wide-beam antenna. In either case, the large azimuth distance-to-target increases the sensitivity to along-track phase-centre displacement. Because the Taylor series approximation is inaccurate under these conditions, it is more appropriate to calculate the sensitivity with respect to the Bakhshali approximation:

$$\frac{\partial \Delta r_n}{\partial \delta_x} = \frac{\bar{x} + \zeta_{x,n} - \delta_x}{\bar{r}} - \frac{2(\bar{x} + \zeta_{x,n} - \delta_x)(\gamma_n - \beta_n)}{2\bar{r}(2\bar{r}^2 + \gamma_n - \beta_n)} + \frac{2(\bar{x} + \zeta_{x,n} - \delta_x)(\gamma_n - \beta_n)^2}{4\bar{r}(2\bar{r}^2 + \gamma_n - \beta_n)^2}. \quad (39)$$

While not immediately obvious due to the complexity of the Bakhshali sensitivity equation, the Bakhshali approximation reveals greater sensitivity to azimuth displacement of the phase-centre than suggested by the Taylor series approximation.

### 3.3.2. Non-ideal motion

$$\frac{\partial \Delta r_n}{\partial \zeta_{x,n}} = \frac{\delta_x}{\bar{r}}. \quad (40)$$

The ratio of phase-centre displacement to range-to-target determines how sensitive the residual range is to non-ideal motion. Stated another way, the residual range sensitivity to non-ideal motion grows in a given dimension as the phase-centre displacement in that dimension grows (i.e.  $\delta_x/\bar{r}$  grows larger). For example, if the SAR has very coarse range resolution (thus increasing the possible values for  $\delta_x$ ) then the residual range is more sensitive to any motion outside the linear track. On the other hand, a large range-to-target mitigates this effect. Thus at farther ranges non-ideal motion becomes less of an issue, especially for fine resolutions.

### 3.3.3. Mean position

$$\frac{\partial \Delta r_n}{\partial \bar{x}} = \frac{\delta_x}{\bar{r}} - \frac{\bar{x}\beta_n}{2\bar{r}^3}. \quad (41)$$

For geometries without squint, the sensitivity to mean antenna position (defined in Equation (23)) is small. In azimuth, if  $\bar{x}$  is small (or zero, as in the case of no squint) then  $\frac{\partial}{\partial \bar{x}} \approx \frac{\delta_x}{\bar{r}}$ , which is the same sensitivity as  $\frac{\partial}{\partial \zeta_{x,n}}$  above. In general this value is small. In range and elevation, the second term significantly reduces the magnitude of the first. Thus, the sensitivity due solely to the magnitude of the mean position is insignificant. The elements dominating the residual range are from Equations (38) and (40) above.

With the general concepts of sensitivity in place, the performance of time-domain back-projection is explored in greater detail in the next section.

## 4. Performance considerations

The following subsections analyse various factors that affect the performance of time-domain back-projection: digital elevation map (DEM) accuracy, antenna position accuracy, azimuth beamwidth, squint, and interpolation of the range-compressed signal. A key concept throughout is that variations in residual phase cause phase errors that can lead to reduced performance.

As previously noted, the physical centre and phase-centre of a scattering-cell are not collocated in general. This leads to a residual phase when the matched filter corresponds to the centre of the cell. As seen in the previous section, if the antenna's azimuth beamwidth is sufficiently narrow then the residual phase due to phase-centre displacement does not vary significantly with pulse number so the net phase error is small. However, if there are errors in DEM height or antenna position measurement, or non-linear platform motion, then the phase error increases.

### 4.1. Digital elevation map

This subsection considers how the accuracy of the DEM affects the back-projected image. The effects vary based on the nature of the platform motion and any uncertainty in knowledge of the platform positions. The case of ideal, linear platform motion is

presented first, followed by more complex models. Recall that back-projected images are formed directly in the ground-plane.

#### 4.1.1. Ideal, linear path

The back-projection formula requires knowing the range from antenna to scattering-cell at every pixel in the image, for every contributing pulse. Assuming the platform positions are already known, the range is calculated for the scattering-cell's three-dimensional location. *A priori* knowledge of the cell's vertical position is provided via a DEM of the terrain. Knowledge of the lateral position is derived from the platform position data and image grid. A height offset (i.e. a bias error) in the elevation map results in varying effects on the output image depending on the SAR collection geometry.

For the simplest case, assume that a non-squinted SAR platform has a straight and level flight track. In this scenario, all platform motion is in the along-track direction (i.e. there is no deviation from the linear path in elevation or cross-track). Recall from Equation (23) that the range to a scattering-cell is  $r_n = \sqrt{x_n^2 + y_n^2 + z_n^2}$ . Considering the motion to be ideal,  $y_n$  and  $z_n$  are constant. Let

$$\bar{r}^2 = \bar{y}_n^2 + \bar{z}_n^2, \quad (42)$$

then

$$r_n = \sqrt{x_n^2 + \bar{r}^2}, \quad (43)$$

which varies in slow-time by azimuth position  $x_n$ . Given a slant-range  $r_n$  and azimuth position  $x_n$ , the potential distances for ground-range  $y$  and elevation  $z$  are not unique. This means that while the slant-range from the SAR to a point on the ground is unique, the potential values for ground-range and elevation of the target lie on a hyperbolic curve given by Equation (42), any point on which provides a correct solution of the slant-range to target. Hence, each range/elevation solution produces an equally well-focused pixel in the back-projected image. However, the elevation offset causes the position of the target in the output image to be translated (i.e. shifted). This is illustrated in Figure 4, where three DEM heights and the respective lateral shift of the target are shown.

A positive vertical offset in the elevation map places the ground-plane closer to the SAR in elevation. As the slant-range solution for a target is constant, this causes the focused target to appear imaged farther away in ground-range. In the same way, lowering the elevation map causes the focused target to appear imaged closer to the SAR in ground-range. Thus, unless the elevation map specifies the correct terrain height, imaged targets are erroneously shifted in range. However, as discussed below, the target's focus is minimally affected for ideal motion. Note that an offset in the elevation map does not affect the azimuth position of the target in the back-projected image, since the along-track dimension is orthogonal to the slant-range dimension.

An offset in the DEM adds approximately a constant range residual at every pulse, and thus approximately the same phase. This is seen in Equation (33). For small DEM errors, given that  $\bar{z} \gg \zeta_{z,n}$  and  $\bar{z} \gg \delta_z$ , the change in  $\Delta r_n$  is approximately the same for every pulse. As the phase added is roughly constant, it has little effect on compression – it is the variation in residual phase that lead to phase errors. However, as the DEM errors increase,

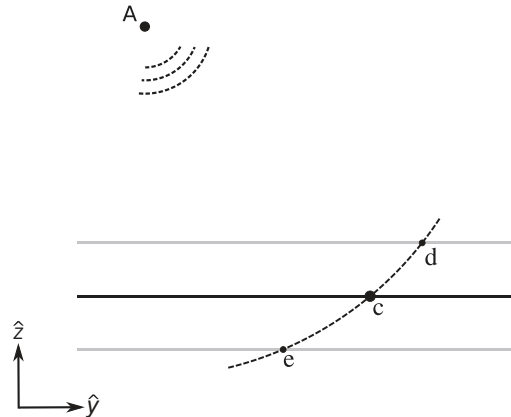


Figure 4. Illustration of lateral shift caused by DEM height offset. An antenna is located at point A and the true DEM height is given by the dark middle line. The dashed curve represents the constant slant-range line. Point c is the correct position of a target. The upper and lower lines indicate errors in the height of the DEM. Note the associated horizontal shift in the target position (shown by dots at points d and e).

the fixed residual range approximation no longer holds and the compression suffers. Thus, back-projection requires at least an approximate idea of the height of the scatterers.

An example of the effects of DEM offset on the azimuth impulse response for an ideal path is illustrated in Figure 5, which shows the azimuth impulse response of a simulated point target. The parameters used in the calculation are 0.3 m wavelength, 8.6° azimuth antenna beamwidth (corresponding to 1 m azimuth resolution), and 45° incidence angle. The azimuth antenna pattern is assumed to be a cosine taper. The SAR platform moves in an ideal, linear fashion. In subfigure (a) the point target is placed at the centre of the scattering-cell while in subfigure (b) the target is placed the maximal distance away according to Equations (18) and (19). Each subfigure has three curves: zero vertical displacement of the DEM and  $\pm 10$  m vertical displacement of the DEM (i.e. DEM height error). Examining both plots, the DEM offset has little effect on the azimuth response;

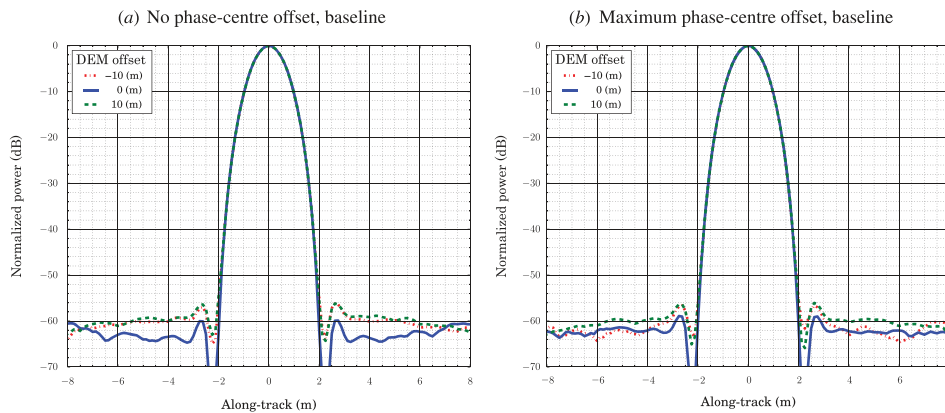


Figure 5. Baseline azimuth impulse response plots. The antenna positions are known exactly on an ideal, linear flight path. Three curves are shown representing different DEM height offsets.

likewise there is little effect on the range response (not shown). While not visible in the figures (because the curves have been shifted to peak at zero), the imaged target positions are shifted in range between the various height curves because the target solution in ground-range changes in order to maintain a constant slant-range to target.

#### 4.1.2. *Known, non-ideal motion*

For the case above, all platform motion is assumed to be in the along-track direction. If motion occurs in the cross-track or elevation directions, then Equation (43) leads to a more constrained estimate for the imaged target position. If the correct height is not used in processing and there is non-ideal motion, then the target's compression suffers. Fortunately, the effect is slight for small height errors.

Figure 6 demonstrates the effects of non-ideal platform motion. Here, the calculation is set up the same as in Figure 5 except that a zero-mean, Gaussian perturbation of standard deviation,  $\sigma_{\text{ant}}$  is added to the antenna positions in range and elevation (the antenna positions are known exactly). The three rows in the figure correspond to position perturbation with a standard deviation of 0.1, 1, and 10 wavelengths and independent from pulse to pulse. While this distribution of platform positions is unlikely for some platforms, the associated analysis estimates the magnitude of the effect of non-ideal motion. For typical SAR pulse repetition frequencies used on typical platforms, even a position deviation as large as 0.1 wavelength may be unrealistic. However, the simple model used here is not intended to be physical, but rather an indicator of how known, non-ideal motion affects back-projection. In addition, for rotary-wing aircraft with slow forward velocity, these larger deviations can occur. The first column gives the azimuth response where the point target is at the physical centre of the scattering-cell and the second column gives the response where it is maximally displaced. Curves for DEM offset of zero and  $\pm 10$  m in elevation are shown. All plots have been normalized to the same peak power in order to compare magnitude effects among the plots.

In the first column of subplots, the target is placed at the physical centre of the cell. When the DEM offset is zero (the solid curves) there is little difference between the mainlobe responses, although there is a raising of the sidelobes as the perturbation increases. In the case with DEM offset where  $\sigma_{\text{ant}} = 1\lambda$ , the peak power is barely affected but the sidelobe level rises 30 dB. At  $\sigma_{\text{ant}} = 10\lambda$  the mainlobe becomes indistinguishable from the sidelobes. This underscores the powerful effect a DEM offset has when the path motion is non-ideal, even for relatively small deviations.

In the case of non-ideal motion, displacing the target to the edge of the cell has the greatest effect in cases where there is no DEM offset. In these cases, the sidelobe level rises significantly. In offset DEM cases, the change in response is insignificant. This suggests that for large DEM errors, the DEM errors dominate the degradation in impulse response while that due to phase-centre displacement is negligible.

#### 4.2. *Antenna position estimate*

DEM uncertainties are not the only sources of geometry error. The position estimates of the antenna are also subject to error. In the previous section it is assumed that the antenna positions are known exactly; now the case of uncertainty in the position estimates is treated. Unknown errors in the antenna position estimate may be classified into two categories: absolute and relative errors. Absolute errors are translations of the entire set of position estimates (e.g. GPS reporting an incorrect, fixed offset in altitude across all

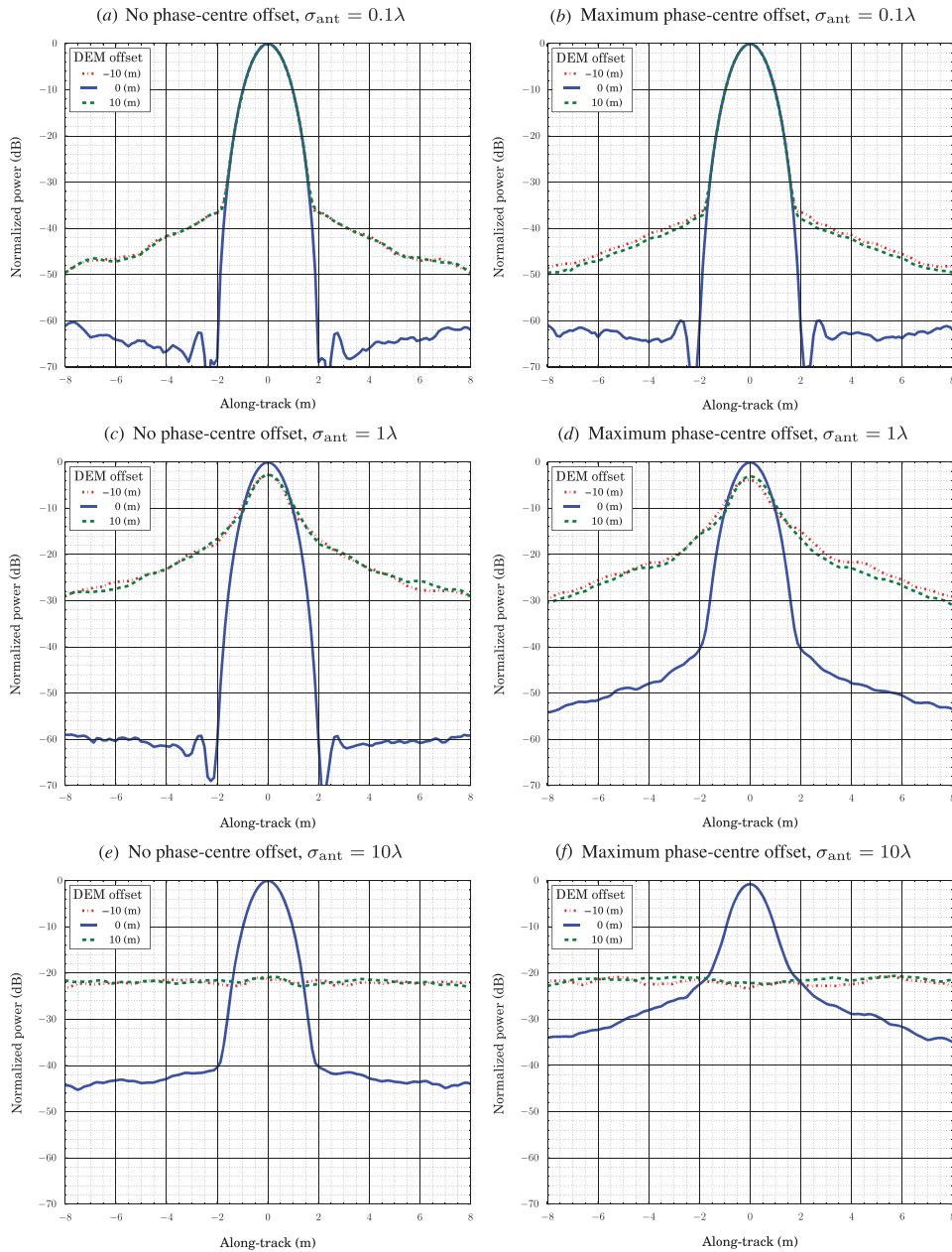


Figure 6. Azimuth impulse response with Gaussian position variance of  $\sigma_{\text{ant}}^2$  in range and elevation. The antenna positions are known exactly. Three curves are shown representing DEM height offsets. The phase-centre offset mostly affects the sidelobes, not the main lobe.

data). Relative errors, on the other hand, are dynamic errors that change over time (e.g. measurement noise or drift).

Absolute position errors are functionally similar to DEM errors. This is because fixed-altitude errors behave identically to a vertical offset in the DEM and horizontal position

errors behave like lateral translations of the DEM. Depending on the scene topography, a lateral translation of the DEM may have no effect (e.g. perfectly flat terrain) or a very large one (e.g. terrain with high relief). Because vertical translation is the same as vertical DEM offset and horizontal translation is scene dependent, no example figures are given here. In general, however, absolute position errors do not cause a reduction in image quality if the magnitude of error is bounded by those common to high-precision GPS (i.e. the GPS absolute position error is smaller than the DEM posting). Since absolute position errors add roughly the same residual phase to each back-projection summation term, they have minimal effect on the result.

Relative position errors, on the other hand, are more problematic because these add a different phase to each term in the back-projection summation. The remainder of this subsection explores the effect of two types of relative position error: Gaussian random noise and drift.

#### 4.2.1. Gaussian random noise

Figure 7 demonstrates the effect of uncertainty on the antenna position. Here, an ideal, linear flight track is assumed during processing using the same parameters as the subsections above, except that noise is added to the antenna positions. This has the effect of adding error to the range calculation. The noise is zero-mean, Gaussian distributed with standard deviations  $\eta_{\text{ant}} = \frac{1}{100}\lambda$ ,  $\frac{1}{16}\lambda$ ,  $\frac{1}{8}\lambda$ , and  $\frac{1}{4}\lambda$ , as shown in Figure 7(a)–(d), respectively. Even with only  $\frac{1}{100}\lambda$  of added noise, and although the mainlobe is unaffected, there is a significant raising of the sidelobes. At  $\frac{1}{16}\lambda$  there is noticeable jump in sidelobe level and the peak also drops by 3 dB. At  $\frac{1}{4}\lambda$  the mainlobe is indistinguishable from the sidelobes.

These plots illustrate the importance of precise knowledge of the relative positions of the antenna (the absolute positions are not as critical for the reasons previously stated). Even tiny levels of uncertainty have a strong effect on impulse response. It is interesting to note that since the antenna position errors dominate, a DEM offset in these cases is almost imperceptible. Although not shown, this is also the case with an offset phase-centre: the effect of scattering-cell phase-centre displacement is imperceptible. For typical SAR inertial navigation systems (INSs), Gaussian random noise on position estimates is not the dominant source of error: errors such as drift are much more significant.

#### 4.2.2. Position drift

Another form of position error is drift. Navigation systems typically employ an inertial measurement unit (IMU). As these sensors generate estimates by integrating accelerometer measurements, drift is almost unavoidable. Not only does drift result in an incorrect estimate of the range-to-target, but it also leads to selecting an incorrect range-migration curve (i.e. the wrong contributions are used in back-projection summation). The magnitude of the effect on imagery corresponds to the magnitude of the drift.

Antenna beamwidth is an important factor in determining vulnerability to drift error because a wider beamwidth leads to a longer synthetic aperture which is more sensitive to drift. Particularly troublesome is drift in the along-track direction as this leads to a larger error in selecting the range-migration curve (i.e. the samples used to back-project a given pixel do not follow the range-migration curve for the corresponding scattering-cell). An example of the effect of cross-track drift is illustrated in Figure 8.

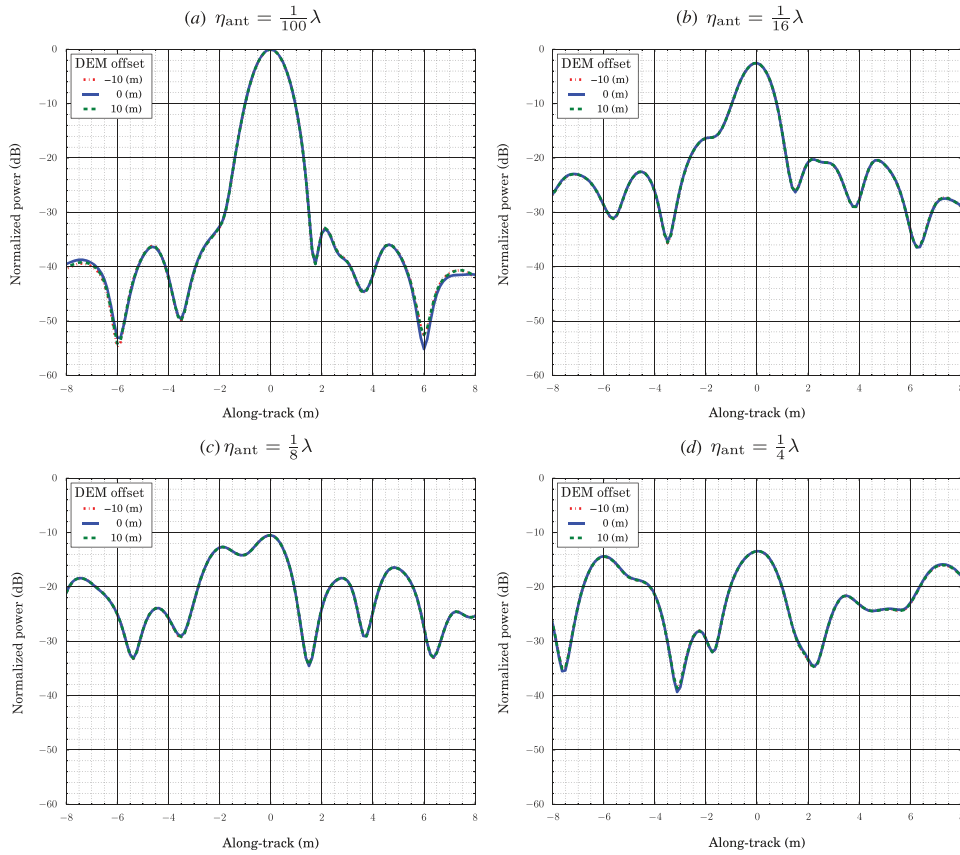


Figure 7. Azimuth impulse response with Gaussian position noise variance of  $\eta_{\text{ant}}^2$  in range elevation. The antenna positions are assumed to lie on an ideal, linear path (corrupted by unknown noise). Three curves are shown representing DEM height offsets. No phase-centre displacement is present.

The effects of antenna position drift are shown in Figure 9. The antenna positions are assumed to be linear (ideal) in the processing, but the actual data has a drift component (i.e. time-varying position error). The fundamental computational parameters are the same as before. The slant-range/azimuth resolutions are each 1 m. Subfigure (a) shows the result when no drift is present. Subfigures (b) and (c) show drift in different dimensions as a function of total magnitude of drift in wavelengths across the synthetic aperture. In (b), 10 wavelengths of position drift in the elevation dimension have a small effect on azimuth IPR: a slight raising of the sidelobes and an imperceptible broadening of the mainlobe. Although not shown, the same magnitude of drift in the ground-range dimension as elevation dimension has an identical effect (for a 45° incidence angle).

Because drift leads to not following the full range-migration curve of a given cell, the utilized azimuth chirp bandwidth for the cell is diminished, which results in coarser resolution. As in the previous figure showing random noise on position estimates, displacement of the phase-centre appears insignificant as it is dominated by errors in

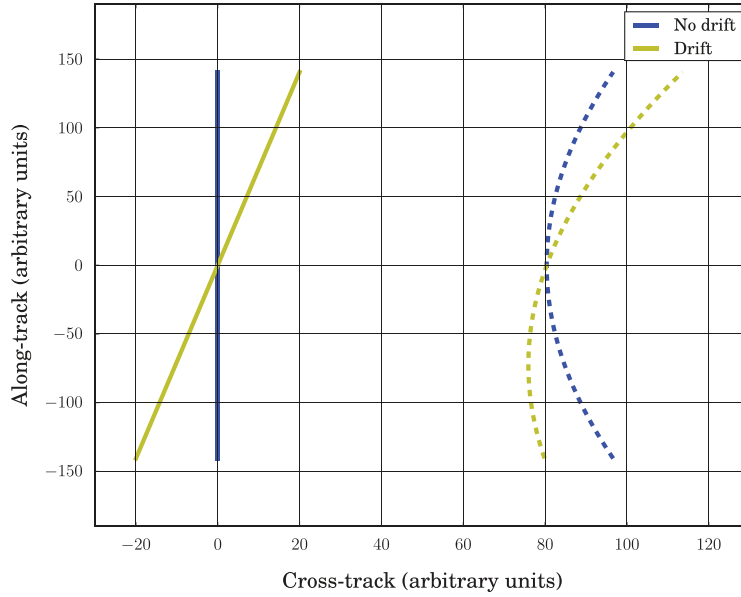


Figure 8. Illustration of the effect of drift on range cell migration. The figure presents a top-down view of the imaging geometry with the solid lines on the left representing the path the platform travels along and the dashed curves on the right representing the range to a given target for each along-track position of the platform. Units are arbitrary. The curve without drift is hyperbolic and symmetric about the POC approach, exemplifying an ideal range-migration curve (RMC). When platform drift is present (exaggerated in this figure), the range curve is skewed.

the antenna position estimate. As stated previously, the effect of drift in the along-track dimension is greater than the other two dimensions.

Figure 9(d) shows the effect of elevation drift on the azimuth position of the target. In this figure, rather than specifying drift in wavelengths, it is specified in metres where the slant-range and azimuth resolutions are both 1 m. At 20 m of elevation drift across the synthetic aperture, the target is displaced nearly 100 m along-track. Figure 9(e) and (f) show various amounts of drift where the curves have been centred in order to compare their shape. Note that the same magnitude of drift causes substantially more effect when it is in the azimuth dimension as opposed to the range or elevation. (Note the difference in horizontal axis scales between (e) and (f).)

#### 4.3. Azimuth beamwidth

This subsection develops an upper-bound on the usable azimuth beamwidth due to phase errors resulting from the unknown location offset of the scattering-cell phase-centre. As shown above, a residual phase results when the phase-centre is not collocated with the physical centre. This induces a phase error that grows as the platform moves away from the point of nominal residual phase (i.e. the POC approach). When the phase error grows sufficiently large, the pulses may sum destructively.

To analyse this, let the slow-time index  $n = 0$  be the pulse index when the platform is located at the synthetic aperture mean (for the particular target).  $\phi_0$  is then the nominal

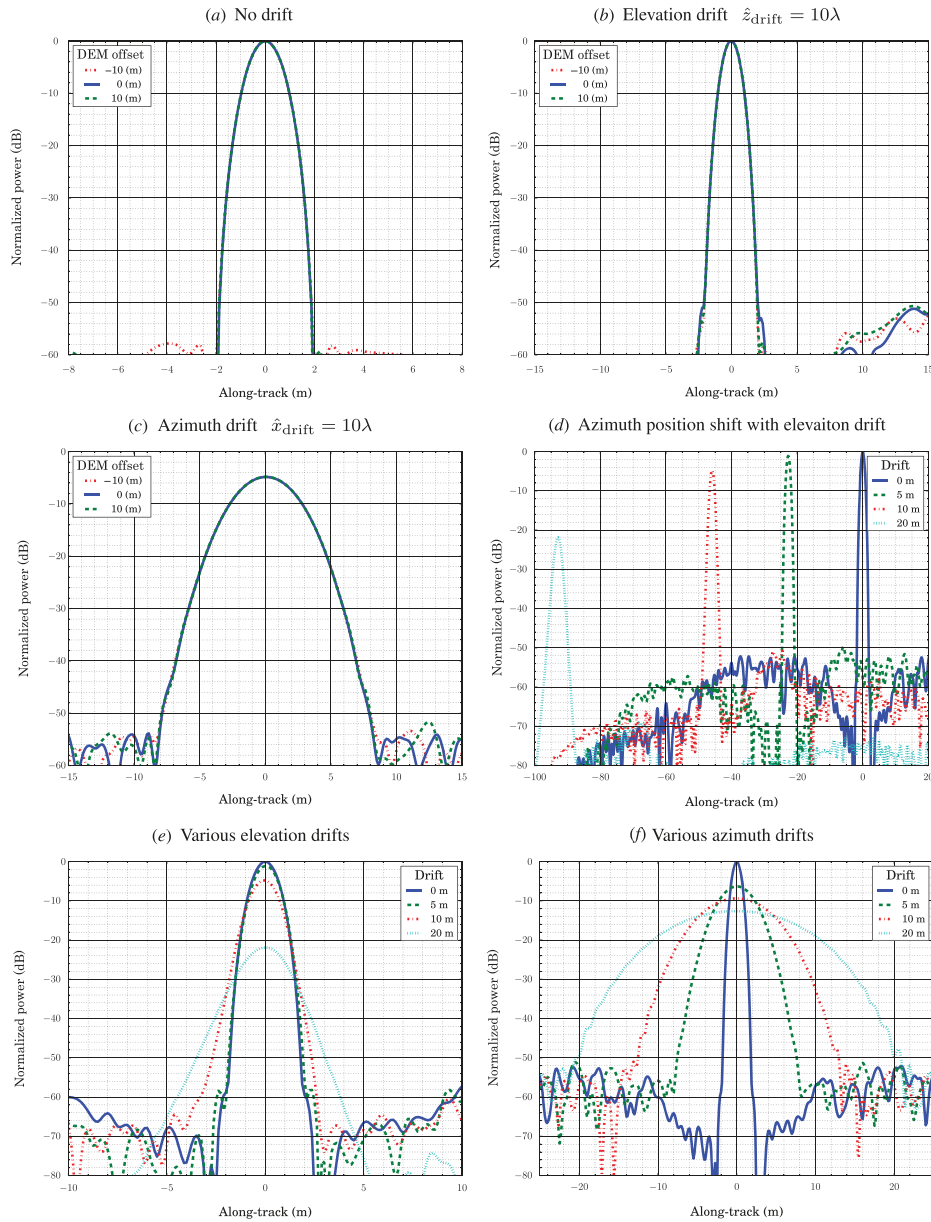


Figure 9. Azimuth impulse response where the antenna positions are assumed to lie on an ideal linear path but the actual positions have drifted in the given dimension; (a) has no drift. In (b) and (c), a drift of  $10\lambda \text{ s}^{-1}$  is present in elevation and azimuth, respectively. In (d)–(f), drift is expressed in total metres across the synthetic aperture.

residual phase corresponding to  $n = 0$ . Destructive summation occurs for a contribution  $\phi_n$  at  $n \neq 0$  when

$$|\phi_n - \phi_0| = \phi_{\text{err}} = \frac{\pi}{2}. \quad (44)$$

In range, this corresponds to

$$\Delta r_{\text{err}} = \frac{\phi_{\text{err}}}{k} = \frac{\lambda}{4}. \quad (45)$$

Because the residual range-induced phase error grows as the platform distance from the mean increases, there exists an azimuth beamwidth wide enough to include target returns that sum destructively if the phase-centre of the cell is sufficiently displaced. Using the approximations of Section 3, it is possible to derive an analytic solution for this maximum azimuth beamwidth.

From Equation (36),  $\gamma_0 = 0$  at the mean. Substituting this in Equation (35), the nominal residual range  $\Delta r_0$  is

$$\begin{aligned} \Delta r_0 &\approx \frac{\beta_0}{2\bar{r}} + \frac{\beta_0^2}{4\bar{r}(2\bar{r}^2 - \beta_0)}, \\ &= \frac{2\beta_0(2\bar{r}^2 - \beta_0) + \beta_0^2}{4\bar{r}(2\bar{r}^2 - \beta_0)}, \\ &= \frac{4\beta_0\bar{r}^2 - \beta_0^2}{4\bar{r}(2\bar{r}^2 - \beta_0)}, \\ &= \frac{\beta_0\left(\bar{r}^2 - \frac{\beta_0}{4}\right)}{2\bar{r}\left(\bar{r}^2 - \frac{\beta_0}{2}\right)}. \end{aligned} \quad (46)$$

This leads to the value  $\phi_0 = k\Delta r_0$ , which is the residual phase at the mean. If  $\beta_0$  is low compared with  $\bar{r}^2$  then

$$\Delta r_0 \approx \frac{\beta_0}{2\bar{r}}, \quad (47)$$

which is the same residual range equation as given by the first-order Taylor series approximation in Equation (32). This confirms the validity of the Taylor series approximation near the POC approach.

According to Equation (45), for contributions away from the nominal (i.e.  $n \neq 0$ ), the point where destructive summation occurs is the maximum residual range  $\Delta r_{\text{max}}$  that is a quarter wavelength away from the residual at the POC approach:

$$\Delta r_{\text{max}} = \Delta r_0 + \frac{\lambda}{4}. \quad (48)$$

Using Equation (35), we are thus interested in finding the point where

$$\Delta r_{\text{max}} = \Delta r_0 + \frac{\lambda}{4} = \frac{\beta_{\text{max}}}{2\bar{r}} - \frac{\gamma_{\text{max}}^2}{4\bar{r}(2\bar{r}^2 + \gamma_{\text{max}})} + \frac{(\gamma_{\text{max}} - \beta_{\text{max}})^2}{4\bar{r}(2\bar{r}^2 + \gamma_{\text{max}} - \beta_{\text{max}})}. \quad (49)$$

If the motion is ideal (i.e. all motion is in the along-track direction), then

$$\gamma_n = \zeta_{x,n}^2. \quad (50)$$

Likewise, if the geometry is non-squinted and there is little phase-centre displacement in azimuth, then

$$\beta_n \approx \beta_0 = 2(\delta_y \bar{y} + \delta_z \bar{z}) - \delta_y^2 - \delta_z^2. \quad (51)$$

Using these two assumptions it is possible to obtain an analytic expression for the maximum azimuth distance away from the mean for which Equation (48) applies. Solving for  $\gamma_n$  in Equation (35) leads to

$$\gamma_n = \frac{\beta_n}{2} - 2\bar{r}^2 \pm \frac{\sqrt{\beta_n(\beta_n - 4\bar{r}\Delta r_n)(16\bar{r}^4 + 4\beta_n\bar{r}\Delta r_n - \beta_n^2)}}{2(4\bar{r}\Delta r_n - \beta_n)}, \quad (52)$$

$$= \frac{\beta_n}{2} - 2\bar{r}^2 \pm \left( \frac{\beta_n^2}{4} + \frac{4\beta_n\bar{r}^4}{4\bar{r}\Delta r_n - \beta_n} \right). \quad (53)$$

Substituting this result into Equations (50) and (51) yields

$$\zeta_{x,\max}^2 = \frac{\beta_0}{2} - 2\bar{r}^2 + \frac{\beta_0^2}{4} + \frac{4\beta_0\bar{r}^4}{4\bar{r}(\Delta r_0 + \lambda/4) - \beta_0}. \quad (54)$$

The minus sign in  $\pm$  is dropped since this leads to a non-physical solution. For a given phase-centre displacement, this can be used to find the maximum distance of the antenna from the POC approach before the pulses sum destructively. This gives a limit for the maximum azimuth beamwidth of the antenna.

An example of the maximum azimuth beamwidth is illustrated in Figure 10. In subfigure (a), the maximum azimuth beamwidth is plotted as a function of incidence angle to the scattering-cell where the platform motion is ideal. Multiple curves are shown, each depicting a different slant-range resolution in wavelength. The phase-centre displacement is the maximum distance from the physical centre of the scattering-cell (from Equations (18) and (19)). For finer-range resolutions (i.e. the upper curves), a wider azimuth beamwidth is permitted than at coarser resolutions. This is because finer-range resolutions limit the maximum phase-centre displacement and thus decrease the maximum residual phase. This means that it may not be possible to obtain fine azimuth resolution simultaneously with coarse range resolution. As stated previously, in many imaging scenarios, scattering-cells are treated as being distributed targets whose phase-centre is near the physical centre. Therefore in practice, scattering-cells may not have the ‘worst case’ phase-centre offset depicted here; however, for discrete targets, an individual point target (e.g. a corner reflector) may be located anywhere within the scattering-cell and thus may result in a maximum residual phase.

The examination above assumes ideal, linear motion of the antenna platform. When non-ideal motion is present, the fluctuation from the linear path increases the magnitude of the range residuals. This further constrains the azimuth beamwidth. Small incidence angles (those near nadir) are affected more significantly by non-ideal motion. This is shown in Figure 10(b)–(d), which illustrate the effect of non-ideal motion for varying degrees of slant-range deviation.

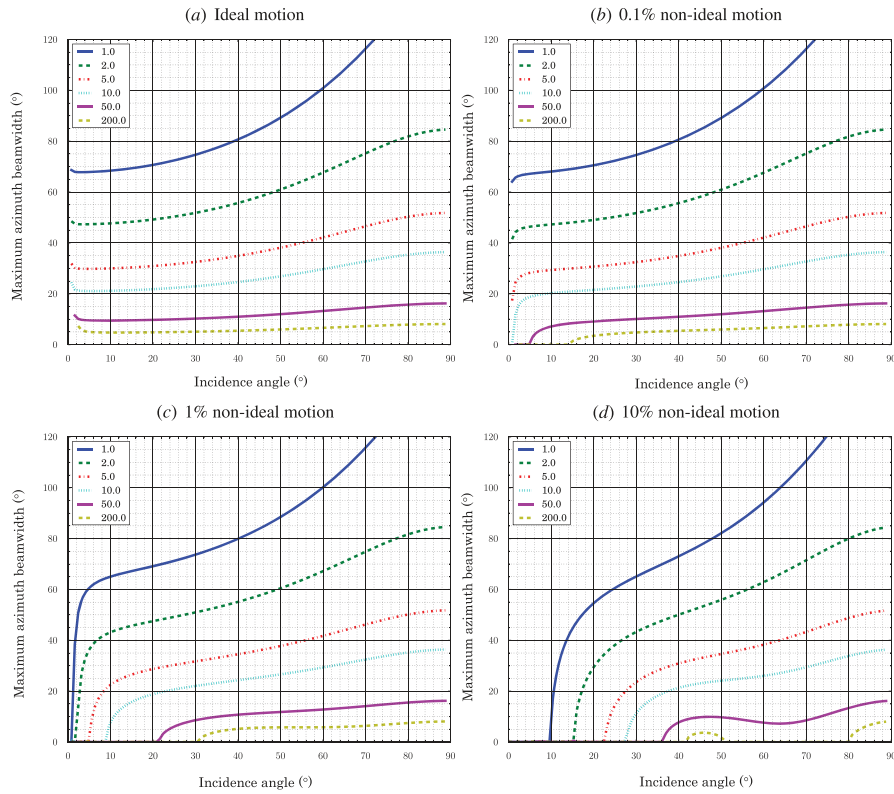


Figure 10. Maximum azimuth beamwidth as a function of incidence angle. In each subfigure, the various curves indicate slant-range resolution in multiples of wavelength. In all cases, the phase-centre of the scattering-cell is located in the corner away from the physical centre. Subfigure (a) shows ideal motion. The remaining subfigures show random non-ideal motion in slant-range, with standard deviation given as a percentage of range to the scattering-cell.

In Figure 10(b), where the displacement is 0.1% of the height above the surface, there is little difference except at low incidence angles ( $<10^\circ$ ) or very coarse range resolutions ( $\sim 200\lambda$ ). When the non-ideal motion is 1% of the height, as in Figure 10(c), the effect of non-ideal motion is more pronounced: the minimum acceptable incidence angle becomes  $20^\circ$ , with the exception of the  $200\lambda$  resolution which has a minimum acceptable incidence angle of  $30^\circ$ . By  $30^\circ$  incidence the maximum beamwidth is identical to that without non-ideal motion for all but the  $200\lambda$  case.

Figure 10(d) shows curves similar to the previous cases when there is 10% height-to-lateral/elevation random path deviation. With this amount of motion the results are highly dependent on the incidence angle. Incidence angles less than  $10^\circ$  are unacceptable at any resolution. At phase-centre displacements of  $200\lambda$ , only a very narrow beamwidth is allowed over a small range of incidence angles.

In most imaging situations the limit on azimuth beamwidth is not an issue. However, there are cases where this issue could arise, especially in low-altitude SAR. For example, if a SAR platform is 500 m above the ground and is imaging at  $40^\circ$  incidence with a  $20^\circ$  beamwidth antenna, then the aperture is 230 m wide. If the platform is travelling in the along-track direction at  $25 \text{ m s}^{-1}$ , then a  $10 \text{ m s}^{-1}$  cross-track velocity causes a residual

phase error large enough that the pulses on the edge of the aperture add destructively for any cells whose phase-centre is 20 or more wavelengths away from the centre of the cell. While the effect may not be dramatic (as it may only affect a relatively small percentage of pulses), it can limit the effective maximum azimuth resolution and potentially introduce artefacts.

#### 4.4. Squint

Squint-mode SAR is where the antenna pointing angle is not coincident with the zero Doppler plane. Where the squint is zero, the antenna points directly at a target when at the POC approach (i.e. when the target is in the zero Doppler plane).

As cited previously, frequency domain algorithms typically require special processing in order to form images from squinted raw data. This arises for two main reasons. First, squint shifts the azimuth chirp spectrum so that it is no longer centred at 0 Hz. This necessitates modification of the azimuth-matched filter. Second, the range and azimuth dimensions begin to couple and are no longer orthogonal, which has differing effects on the algorithms depending on the nature of their treatment of orthogonality. The effects become especially pronounced at larger squint angles ( $>30^\circ$ ).

Because back-projection models the propagation phase of the expected received signal as part of the matched filter, squint-mode operation does not require special treatment. In other words, back-projection natively forms images from even highly squinted geometries; the Doppler-centroid shift needs no special handling even if aliased. For further discussion on this, see Duersch (2013).

## 5. Discussion

Back-projection may be seen as an ideal two-dimensional, spatially varying matched filter. It is particularly suited to low-altitude, high-motion scenarios. If the imaging geometry is known exactly then back-projection is exact. Unfortunately, this is rarely the case since the phase-centre of the scattering-cells is unknown and there is inaccuracy in the measurement of the platform position. These uncertainties lead to phase errors that distort the back-projection solution. Fortunately, however, these errors are generally small.

As shown in Section 4.1, for common slant-range resolutions, the effect of having the phase-centre located away from the physical centre of the scattering-cell is minimal when DEM error is small. Since high-quality DEMs are available over many parts of the Earth, this requirement is often met. In addition, considering that many imaging scenarios involve distributed targets whose phase-centre is near the physical centre of the cell, this issue is further moderated for such targets (although discrete targets may still be affected).

Another issue affecting system performance is the quality of position estimates from the navigation system. Even when corrected using satellite data, navigation systems are subject to drift in the position estimates. Because the synthetic aperture length increases with height above the imaged scene, so does the magnitude of drift. Thus, a more precise navigation system may be required at higher altitudes. This limitation, however, may be relaxed through the use of autofocus techniques. Autofocus algorithms are commonly used in SAR to remove phase errors due to uncompensated motion, hardware limitations, or other non-ideal effects (Carrara, Goodman, and Majewski 1995; Mancill and Swiger 1981; Eichel, Ghiglia, and Jakowatz 1989; Werness et al. 1990; Wahl et al. 1994; Li, Guosui, and Jinlin 1999; Fienup and Miller 2003).

DEM and INS accuracy help determine whether back-projection is well suited to a given situation. In addition, the imaging scenario helps determine suitability. In space-borne applications, the platform motion is very regular (i.e. nearly ideal), has very large range-to-target, and generally has a narrow enough range swath that the change in incidence angle across the swath is minor. Thus, at high altitudes, frequency domain methods are recommended since these are more computationally efficient. On the other hand, at low altitudes there may be significant non-ideal motion, high range-migration, dynamic imaging modes, etc. Thus, the highly parametrizable matched filter of back-projection becomes advantageous when imaging at low altitudes, and particularly at very low altitudes (i.e. tens or hundreds of metres above the ground).

## 6. Conclusion

This article explores time-domain back-projection for stripmap SAR from first principles. The back-projection algorithm may be advantageous in imaging situations consisting of a high degree of non-ideal motion (e.g. very low altitude, small platform). Several methods of approximating the hyperbolic range-to-target are provided and compared. Using these approximations, this article presents an analysis of the sensitivity of back-projection to its geometric inputs as well as several performance considerations. It is seen that the sensitivity to motion, range, etc. in a given dimension is higher the more the phase-centre is displaced from the pixel centre in that dimension. Increasing the slant-range to target desensitizes the residuals with respect to motion and phase-centre displacement. Narrow-beam antennas are not as sensitive to small along-track phase-centre displacement. It is seen that the required DEM accuracy for back-projection is dependent on the level of non-ideal motion present: more non-ideal motion requires a more accurate DEM to produce the same quality of imagery.

## Disclosure statement

No potential conflict of interest was reported by the authors.

## References

- Bamler, R. 1992. "A Comparison of Range-Doppler and Wavenumber Domain SAR Focusing Algorithms." *IEEE Transactions on Geoscience and Remote Sensing* 30 (4): 706–713. doi:10.1109/36.158864.
- Benz, U., K. Strodl, and A. Moreira. 1995. "A Comparison of Several Algorithms for SAR Raw Data Compression." *IEEE Transactions on Geoscience and Remote Sensing* 33 (5): 1266–1276. doi:10.1109/36.469491.
- Carrara, W. G., R. S. Goodman, and R. M. Majewski. 1995. *Spotlight Synthetic Aperture Radar: Signal Processing Algorithms*. Norwood, MA: Artech House.
- Caves, R., S. Quegan, and R. White. 1998. "Quantitative Comparison of the Performance of SAR Segmentation Algorithms." *IEEE Transactions on Image Processing* 7 (11): 1534–1546. doi:10.1109/83.725361.
- Channabasappa, M. N. 1976. "On the Square Root Formula in the Bakhshali Manuscript." *Indian Journal History Sciences* 2: 112–124.
- Cumming, I., and J. R. Bennett. 1979. "Digital Processing of SEASAT SAR Data." *IEEE International Conference on Acoustics, Speech, and Signal Processing, ICASSP '79* 4: 710–718.
- Cumming, I. G., and F. H. Wong. 2005. *Digital Processing of Synthetic Aperture Radar Data*. London: Artech House.

- D'Aria, D., and A. M. Guarnieri. 2007. "High-Resolution Spaceborne SAR Focusing by SVD-Stolt." *IEEE Geoscience and Remote Sensing Letters* 4 (4): 639–643. doi:10.1109/LGRS.2007.903081.
- Duersch, M. I. 2013. "Backprojection for Synthetic Aperture Radar." PhD thesis, Brigham Young University.
- Duersch, M. I., and D. G. Long. 2015. "Analysis of Multi-static Pixel Correlation in SAR." *IEEE Transactions on Geoscience and Remote Sensing* 53: 362–374. doi:10.1109/TGRS.2014.2322611.
- Eichel, P. H., D. C. Ghiglia, and C. V. Jakowatz Jr. 1989. "Speckle Processing Method for Synthetic-Aperture-Radar Phase Correction." *Optics Letters* 14 (1): 1–3.
- Eldhuset, K. 1998. "A New Fourth-Order Processing Algorithm for Spaceborne SAR." *IEEE Transactions on Aerospace and Electronic Systems* 34 (3): 824–835. doi:10.1109/7.705890.
- Fienup, J. R., and J. J. Miller. 2003. "Aberration Correction by Maximizing Generalized Sharpness Metrics." *Journal Optical Society American* 20 (4): 609–620.
- Gilmore, C., I. Jeffrey, and J. LoVetri. 2006. "Derivation and Comparison of SAR and Frequency-Wavenumber Migration within a Common Inverse Scalar Wave Problem Formulation." *IEEE Transactions on Geoscience and Remote Sensing* 44 (6): 1454–1461. doi:10.1109/TGRS.2006.870402.
- Jin, M. Y., and C. Wu. 1984. "A SAR Correlation Algorithm Which Accommodates Large-Range Migration." *IEEE Transactions on Geoscience and Remote Sensing* GE-22: 592–597. doi:10.1109/TGRS.1984.6499176.
- Li, X., L. Guosui, and N. Jinlin. 1999. "Autofocusing of ISAR Images Based on Entropy Minimization." *IEEE Transactions on Aerospace and Electronic Systems* 35 (4): 1240–1252. doi:10.1109/7.805442.
- Mancill, C. E., and J. M. Swiger. 1981. "A Map Drift Autofocus Technique for Correcting Higher-Order SAR Phase Errors." In *27th Annual Tri-Service Radar Symposium Record*, 391–400, Monterey, CA, June 23–25.
- Mittermayer, J., A. Moreira, and O. Loffeld. 1999. "Spotlight SAR Data Processing Using the Frequency Scaling Algorithm." *IEEE Transactions on Geoscience and Remote Sensing* 37 (5): 2198–2214. doi:10.1109/36.789617.
- Moreira, A., J. Mittermayer, and R. Scheiber. 1996. "Extended Chirp Scaling Algorithm for Air- and Spaceborne SAR Data Processing in Stripmap and Scansar Imaging Modes." *IEEE Transactions on Geoscience and Remote Sensing* 34 (5): 1123–1136. doi:10.1109/36.536528.
- Prats, P., K. A. C. de Macedo, A. Reigber, R. Scheiber, and J. J. Mallorqui. 2007. "Comparison of Topography- and Aperture-dependent Motion Compensation Algorithms for Airborne SAR." *IEEE Geoscience and Remote Sensing Letters* 4 (3): 349–353. doi:10.1109/LGRS.2007.895712.
- Prats-Iraola, P., R. Scheiber, M. Rodriguez-Cassola, J. Mittermayer, S. Wollstadt, F. De Zan, B. Brautigam, M. Schwerdt, A. Reigber, and A. Moreira. 2014. "On the Processing of Very High Resolution Spaceborne SAR Data." *IEEE Transactions on Geoscience and Remote Sensing* 52 (10): 6003–6016. doi:10.1109/TGRS.2013.2294353.
- Raney, R. K., H. Runge, R. Bamler, I. G. Cumming, and F. H. Wong. 1994. "Precision SAR Processing Using Chirp Scaling." *IEEE Transactions on Geoscience and Remote Sensing* 32 (4): 786–799. doi:10.1109/36.298008.
- Ribalta, A. 2011. "Time-Domain Reconstruction Algorithms for FMCW-SAR." *IEEE Geoscience and Remote Sensing Letters* 8 (3): 396–400. doi:10.1109/LGRS.2010.2078486.
- Richards, M. A. 2005. *Fundamentals of Radar Signal Processing*. New York: McGraw-Hill.
- Rocca, F. 1987. "Synthetic Aperture Radar: A New Application for Wave Equation Techniques." *Stanford Exploration Project Reports* SEP-56: 167–189.
- Rodriguez-Cassola, M., P. Prats-Iraola, F. De Zan, R. Scheiber, A. Reigber, D. Geudtner, and A. Moreira. 2015. "Doppler-Related Distortions in TOPS SAR Images." *IEEE Transactions on Geoscience and Remote Sensing* 53 (1): 25–35. doi:10.1109/TGRS.2014.2313068.
- Sun, G., M. Xing, Y. Liu, L. Sun, Z. Bao, and Y. Wu. 2011. "Extended NCS Based on Method of Series Reversion for Imaging of Highly Squinted SAR." *IEEE Geoscience and Remote Sensing Letters* 8 (3): 446–450. doi:10.1109/LGRS.2010.2084562.
- Ulander, L. M. H., H. Hellsten, and G. Stenstrom. 2003. "Synthetic-Aperture Radar Processing Using Fast Factorized Back-Projection." *IEEE Transactions on Aerospace and Electronic Systems* 39 (3): 760–776. doi:10.1109/TAES.2003.1238734.

- Vu, V. T., T. K. Sjogren, and M. I. Pettersson. 2008. "A Comparison between Fast Factorized Back-projection and Frequency-Domain Algorithms in UWB Lowfrequency SAR". *Proceedings IEEE International Geoscience and Remote Sensing Symposium IGARSS*, Vol. 4, Boston, MA, June 7–11, 1284–1287. doi:10.1109/IGARSS.2008.4779965.
- Vu, V. T., T. K. Sjogren, and M. I. Pettersson. 2011. "Fast Backprojection Algorithm for UWB Bistatic SAR." *Proceedings IEEE Radar Conference (RADAR)*, Kansas City, MO, May 23–27, 431–434. doi:10.1109/RADAR.2011.5960575.
- Wahl, D. E., P. H. Eichel, D. C. Ghiglia, and C. V. Jakowatz Jr. 1994. "Phase Gradient Autofocus-A Robust Tool for High Resolution SAR Phase Correction." *IEEE Transactions on Aerospace and Electronic Systems* 30 (3): 827–835. doi:10.1109/7.303752.
- Werness, S. A. S., W. G. Carrara, L. S. Joyce, and D. B. Franczak. 1990. "Moving Target Imaging Algorithm for SAR Data." *IEEE Transactions on Aerospace and Electronic Systems* 26 (1): 57–67. doi:10.1109/7.53413.
- Zaugg, E. 2010. "Generalized Image Formation for Pulsed and LFM-CW Synthetic Aperture Radar." PhD thesis, Brigham Young University.
- Zaugg, E. C., and D. G. Long. 2009. "Generalized Frequency-Domain SAR Processing." *IEEE Transactions on Geoscience and Remote Sensing* 47 (11): 3761–3773. doi:10.1109/TGRS.2009.2025372.
- Zaugg, E. C., and D. G. Long. 2015. "Generalized Frequency Scaling and Backprojection for LFM-CW SAR Processing." *IEEE Transactions on Geoscience and Remote Sensing* 53: 3600–3614. doi:10.1109/TGRS.2014.2380154.